RESEARCH ARTICLE | JUNE 09 2025

The pore-network-continuum hybrid modeling of nonlinear shale gas flow in digital rocks of organic matter *⊗*

Dongchen Liu (刘东晨) ➡ ⑩ ; Xuefeng Yang (杨学峰); Deliang Zhang (张德良); Shan Huang (黄山); Rui Jiang (蒋睿); Jianqi Rong (荣健淇); Zhiwei Wang (王志伟); Bowen Shi (史博文); Chao-Zhong Qin (秦朝中) ➡ ⑩



Physics of Fluids 37, 063608 (2025) https://doi.org/10.1063/5.0265700





Articles You May Be Interested In

Calculation model of shale fracture compressibility and evolution of permeability under water-bearing conditions

Physics of Fluids (November 2024)

Impact of reservoir pressure fluctuations on fracture shear slip behavior in shale gas hydraulic fracturing Physics of Fluids (December 2024)

Dynamic coupling mechanism of shale drilling fluid invasion depth, fracture width, and rock strength Physics of Fluids (June 2025)



Physics of Fluids

Special Topics Open for Submissions

Learn More



The pore-network-continuum hybrid modeling of nonlinear shale gas flow in digital rocks of organic matter

Cite as: Phys. Fluids **37**, 063608 (2025); doi: 10.1063/5.0265700 Submitted: 15 February 2025 · Accepted: 22 April 2025 · Published Online: 9 June 2025







Dongchen Liu (刘东晨),^{1,2,3,3)} D Xuefeng Yang (杨学峰),^{1,2} Deliang Zhang (张德良),^{1,2} Shan Huang (黄山),^{1,2} Rui Jiang (蒋睿),^{1,2} Jianqi Rong (荣健淇),⁴ Zhiwei Wang (王志伟),⁴ Bowen Shi (史博文),⁴ and Chao-Zhong Qin (秦朝中)^{4,3} D

AFFILIATIONS

- ¹Shale Gas Research Institute, PetroChina Southwest Oil & Gasfield Company, Chengdu, Sichuan Province, China
- ²Shale Gas Evaluation and Exploitation Key Laboratory of Sichuan Province, Chengdu, Sichuan Province, China
- ³State Key Laboratory of Oil and Gas Reservoir Geology and Exploitation, Southwest Petroleum University, Chengdu, Sichuan Province, China
- School of Resources and Safety Engineering, Chongqing University, Chongqing, China

ABSTRACT

Organic matter (OM) serves as the primary source of gaseous hydrocarbons in shales. Fundamental understanding of its permeability and gas production characteristics is vital to optimize shale gas exploitation. The focused ion beam scanning electron microscopy (FIB-SEM) imaging can resolve OM macropores with pore radii ranging from tens to hundreds of nanometers, while pore sizes of sub-resolution OM can be characterized using low-temperature gas adsorption. In this work, we focus on multiscale pore structures of OM and contribute to the development of an efficient pore-network-continuum model for simulating nonlinear gas flow in multiscale OM digital rocks, along with its fully coupled implicit numerical implementation. To demonstrate the influence of OM pore structures on its permeability and transient gas production, we select three types of OM featured by their distinct porosities, connectivity of macropores, and pore morphologies. We show that the high-porosity OM with interconnected macropores exhibits markedly different intrinsic permeability, mechanisms of apparent permeability, gas storage, and production behaviors compared to the medium-porosity and low-porosity OM. Moreover, we propose an empirical formula for OM apparent permeability with respect to an effective characterization length used in the calculation of Knudsen number, which will be the key input to the representative elementary volume (REV) size modeling of shale matrix.

Published under an exclusive license by AIP Publishing. https://doi.org/10.1063/5.0265700

I. INTRODUCTION

Shale gas has become a key player in the transition from conventional fossil fuels to lower-carbon energy sources for its substantial reserves and successful exploitation (Long et al., 2018; Sun et al., 2021). Moreover, depleted shale formations can be used as cap rocks for carbon storage (Edwards et al., 2015) and repositories for nuclear waste disposal (Joyce et al., 2014). However, due to the highly heterogeneous nature at multiple length scales in terms of pore structures and material constituents (Chalmers et al., 2012; Clarkson et al., 2013; and Sondergeld et al., 2010), understanding the nonlinear, multi-physics coupled gas flow processes (Cheng et al., 2020) in shale matrix, particularly at the representative elementary volume (REV) scale, still remains a challenge and an active area of research.

Digital rock physics (DRP) (Blunt et al., 2013), which uses high-resolution images of rock samples as the input for flow simulations, has been used for shales (Ma et al., 2016; 2019). The "dual-scale" images, including resolved large pores (referred to as macropores) and pores of a size smaller than the image resolution, can be used by various multiscale numerical models. The multiscale models may be broadly classified into three categories, including direct numerical simulations (DNS) (Soulaine et al., 2016), dual-pore-network models (Cui et al., 2022; Xiong et al., 2016), and pore-network-continuum models (Shi et al., 2024; Zhang et al., 2024). It is worth noting that in the porous media research, continuum-scale models usually involve averaged material parameters such as porosity and permeability, whereas DNS models refer to the direct numerical modeling of flow and

^{a)}Authors to whom correspondence should be addressed: dongchen_liu@126.com and chaozhong.qin@cqu.edu.cn

transport in void spaces. First, DNS employs a micro-continuum modeling framework, usually based on the Darcy-Brinkman-Stokes equation (DBS) (Brinkman, 1949; Soulaine and Tchelepi, 2016). This approach solves the Stokes equation for flow in macropores, and applies the Darcy equation to describe flow in sub-resolution regions (referred to as microporosity). Second, dual-pore-network models represent macropores as a pore network of idealized pore elements, while microporosity is either represented by a separate pore network (Jiang et al., 2013; Mehmani and Prodanović, 2014; Prodanović et al., 2015; and Yang et al., 2015) or simplified by effective "pore throats" without resolving the pore structures of microporosity (Bauer et al., 2012; Bultreys et al., 2015). Last, in a pore-network-continuum model, flow in macropores is modeled using the computationally efficient porenetwork approach, while flow in microporosity is descried by the continuum-scale approach, which can capture high-resolution heterogeneity of microporosity (Wu et al., 2017). Notably, Shi et al. (2024) recently developed a multi-level controllable coarsening algorithm for microporosity voxels, which substantially reduces computational grids for the pore-network-continuum modeling.

Over the past few years, there have been many pore-scale numerical studies of nonlinear gas flow in shale matrix (Feng et al., 2024; Guo et al., 2018; Song et al., 2018; 2020; and Zhang et al., 2024). Fully coupled numerical models including gaseous slippage flow, adsorption/ desorption, and surface diffusion of adsorbed methane were developed, to predict apparent permeability and transient gas production (Cheng et al., 2020). Feng et al. (2024) developed a dual-pore-network model for nonlinear gas flow in shale matrix composed of inorganic pores with and without clays, and organic pores. They extensively investigated various parameters such as pore size, coordination number, TOC (total organic content), and clay content on apparent permeability. However, due to the challenge in reconstructing REV-size shale digital rocks, regularized numerical pore networks with a maximum domain size of $18 \,\mu\mathrm{m}$ were used. Song et al. (2018, 2020) used the multiple-point statistics (MPS) method to construct a 3D shale sample from 2D SEM images, and then pore networks were extracted by various methods such as maximal ball filling and medium-axis methods (Blunt et al., 2013; Dong and Blunt, 2009). The authors conducted the sensitivity study of apparent permeability to various parameters by simulating pulse-decay and pressure-drop transient processes. However, their digital rocks constructed stochastically from limited images cannot fully capture the properties of the multi-mineral and multiscale pore structures of shales, may resulting in dissimilarities with the real natural shale samples (Zhu et al., 2019). Guo et al. (2018) developed a micro-continuum model based on the DBS equation in the OpenFOAM®, to simulate nonlinear gas flow in a high-resolution 3D focused ion beam scanning electron microscopy (FIB-SEM) image. Due to the heavy computational efforts, only a subvolume of $3.56 \times 2.5 \times 3.36 \,\mu\text{m}^3$ was modeled, which is much smaller than the REV size of shale matrix (Wu et al., 2020). Zhang et al. (2024) developed a pore-network-continuum model for two-component gas transport in shale sample, i.e., the displacement of methane by CO2. A synthesized shale digital rock was used, and microporosity voxels were used as computational grids directly, which are computationally heavy.

Attempts have been made to address the above issues (Ning et al., 2016; Wu et al., 2017). A "bottom-up" multiscale reconstruction strategy involving FIB-SEM, nano-CT, and micro-CT to simulate the transport properties of shale gas from the nano- to macroscale was

proposed. Empirical formulas, such as the Kozeny-Carman equation (Civan, 2010) with nanoscale effect (Wu and Zhang, 2016), as well as molecular dynamics simulations and LBM (He et al., 2016), are used to obtain the apparent permeability of organic matter (OM) and clay minerals. In organic-rich shale matrix, OM serves as the main source of gaseous hydrocarbons in shales as well as the main migration pathways in exploitation (Gensterblum et al., 2015; Ross and Bustin, 2009). Advanced imaging techniques (Curtis et al., 2012) and lowtemperature gas adsorption (Chalmers et al., 2012; Clarkson et al., 2013; and Sondergeld et al., 2010) have revealed that pore sizes in OM can range from a few nanometers to hundreds of nanometers, creating multiscale pore structures. "Dual-scale" digital images taken from FIB-SEM of OM have shown that macropores themselves may show good connectivity (Wu et al., 2017) or be interconnected by microporosity (Ning et al., 2016). Porosity and connectivity of macropores, respectively, determine the gas storage capacity and intrinsic permeability in OM. Therefore, distinction in different types of OM is the prerequisite of REV-size gas production simulations and apparent permeability predictions, which requires further detailed research.

In this work, we extend our previously developed pore-network-continuum model (Shi et al., 2024) to simulate nonlinear gas flow in multiscale OM digital rocks. The model considers the essential mechanisms of compressibility, slippage flow, adsorption/desorption, and surface diffusion. Moreover, the coarsening of microporosity voxels is implemented to reduce computational efforts. We aim to demonstrate the influence of OM pore structures on its permeability and gas production characteristics. To this end, we select three types of OM featured by their distinct porosities, connectivity of macropores, and pore morphologies. Finally, based on our pore-scale numerical results, we develop an empirical formula for OM apparent permeability with respect to a characterization length used in the calculation of Knudsen number. The developed empirical formula will be the key input to the REV-scale modeling of gas flow in shale matrix.

II. MATERIALS AND METHOD A. Digital rocks of organic matter

Three in situ organic-rich shale samples were taken from the Longmaxi Formation in the Luzhou Block of the Sichuan Basin, which were named as OM-HP, OM-MP, and OM-LP (OM denotes organic matter; HP, MP, and LP denote high-porosity, medium-porosity, and low-porosity, respectively). As shown in Figs. 1(a) and 1(b), the FIB-SEM images show distinct OM pores including filamentous, bubblelike, and sponge-like pores (Ma et al., 2021). We applied the Fast Fourier Transformation (FFT) filtering to the original FIB-SEM images [Fig. 1(a)] to eliminate stripe artifacts. Then, the images were imported into ImageJ (Schneider et al., 2012) and was segmented into subresolution regions (i.e., microporosity), resolved macropores, and solid minerals by using the Trainable Weka Segmentation module (Arganda-Carreras et al., 2017). We selected the largest organic-rich regions [Fig. 1(c)] as our study domains, with a size of 400³ cubic voxels and a resolution of 4 nm. To reduce computational costs, we further reduced the voxel resolution to 32 nm and obtained the final digital rocks of OM, with a size of 50³ cubic voxels as shown in Fig. 1(d). It is worth noting that we numerically compared the intrinsic permeability and the porosity of macropores before and after the resolution reduction. It is found that the resolution reduction impacts the two values to

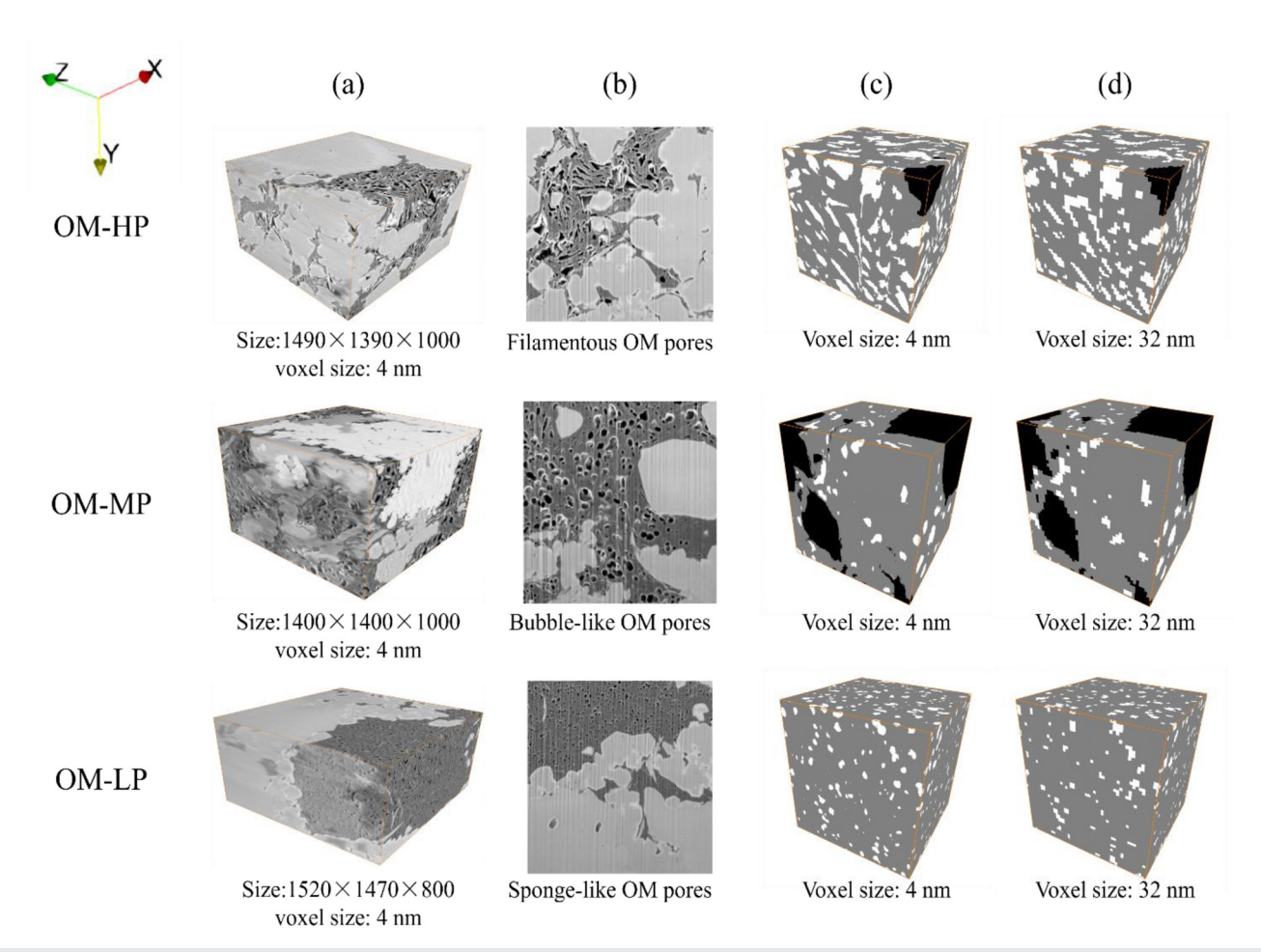


FIG. 1. (a) The FIB-SEM images with a voxel resolution of 4 nm; (b) the 2D cross sections showing distinct OM pores including filamentous, bubble-like, and sponge-like pores; (c) the selected OM regions of 400³ voxels segmented using ImageJ where the white, gray, and black denote macropores, sub-resolution OM microporosity, and solid minerals, respectively; and (d) the final digital rocks of OM used in the numerical modeling which have the size of 50³ voxels with the voxel resolution of 32 nm.

some extent, but does not alter the connectivity of macropores. The details can be found in Appendix C.

Compared to the FIB-SEM imaging, the FIB-HIM (focused ion beam-helium ion microscopy) with a higher resolution of 1 nm can reveal more OM pores (Wu et al., 2023). Moreover, our nitrogen adsorption experiments indicate that nano pores smaller than 4 nm in diameter contribute significantly to the total porosity. To characterize the pore sizes of sub-resolution OM microporosity, we estimated an average pore radius from the data of nitrogen adsorption and carbon dioxide adsorption experiments. Given the voxel resolution of 32 nm, the portion of pore radii smaller than 20 nm in the gas adsorption data was applied, and a volume-averaged pore radius is found to be 3.48 nm. It is worth noting that, as a first attempt, we assume homogenous OM microporosity. By further assuming an average porosity of 10% (Guo et al., 2018), the intrinsic permeability of OM microporosity was calculated to be 12.3 nD using the Katz–Thompson model (Katz and Thompson, 1986).

In the hybrid pore-network-continuum modeling framework for flow and transport in multiscale digital rocks (Shi et al., 2024;

Zhang et al., 2024), first, we extracted the pore network of macropores by the watershed algorithm (Gostick, 2017; Kornilov and Safonov, 2018). Then, the original voxels of OM microporosity were substantially coarsened to be microporosity grids by the algorithm developed in Shi et al. (2024). Finally, the pore network and microporosity grids were geometrically fused to generate the computational mesh, as the input to a pore-network-continuum hybrid model. Figure 2 shows the exemplary workflow for the generation of computational mesh of the digital rock of OM-HP. For more details, one can refer to Shi et al. (2024).

We substantially analyzed the three digital rocks, to understand their key differences in pore structures. Table I lists the key information of OM pore structures. First, it is seen that the three cores have the porosity values of 23.9%, 9.0%, and 7.7% (the revised values are 24.3%, 11%, and 8.1%), corresponding to the digital rocks of OM-HP (high-porosity OM), OM-MP (medium-porosity OM), and OM-LP (low-porosity OM), respectively. We also see that the mean pore size of macropores is positively correlated with the porosity of macropores, and the digital rocks of OM-HP has the largest mean pore size of 135.4 nm. Based on the image analysis, it is found that the filamentous

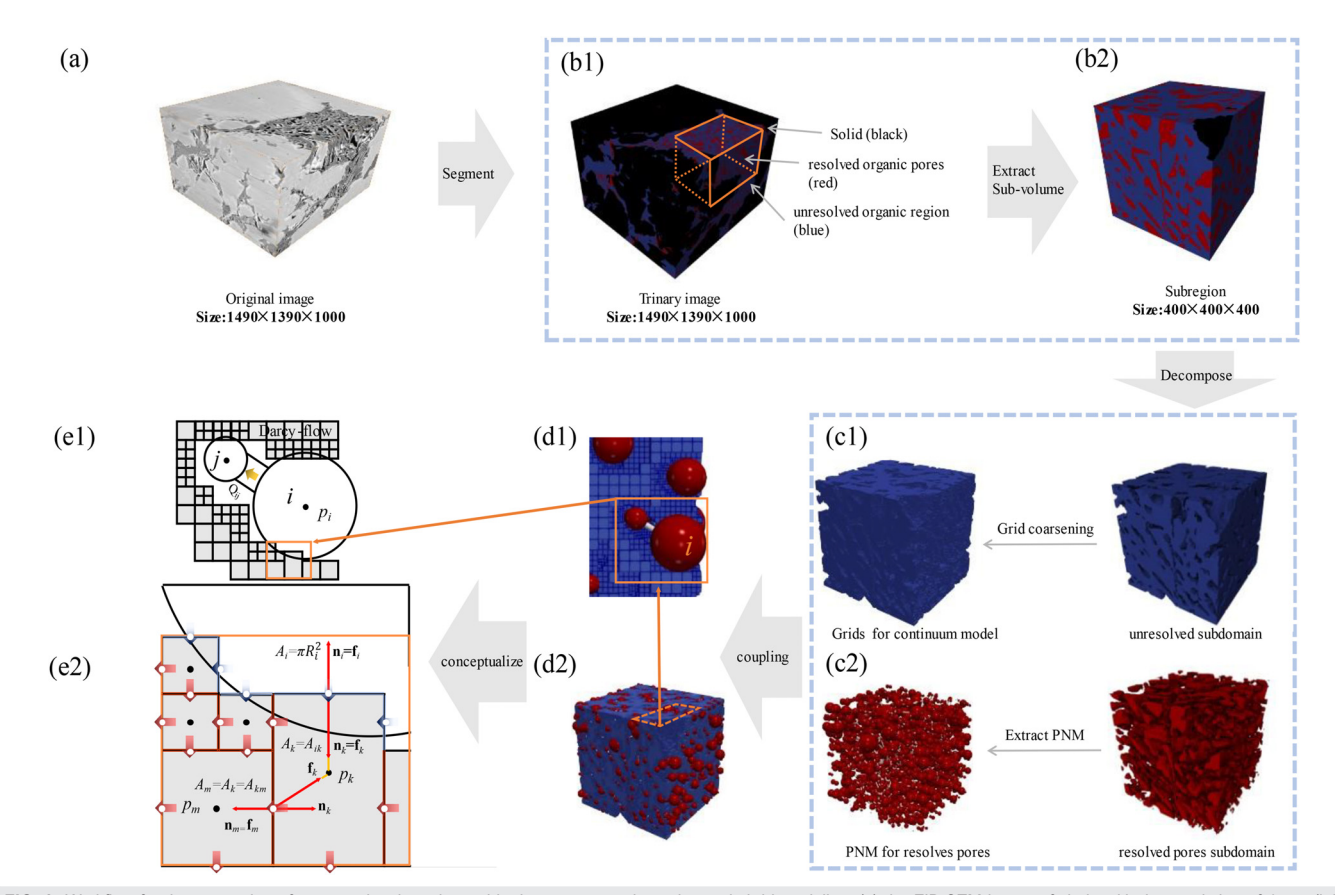


FIG. 2. Workflow for the generation of computational mesh used in the pore-network-continuum hybrid modeling: (a) the FIB-SEM image of shale with the resolution of 4 nm; (b1) the segmented ternary image with black, red, and blue colors denoting solid, resolved macropores, sub-resolution microporosity, respectively; (b2) sub-volume with the size of $400 \times 400 \times 400$; (c1) the generation of coarsened grids in microporosity; (c2) the extracted pore network of macropores; (d2) the computational mesh used in the hybrid modeling; (d1) the zoom-in view; (e1) the interface between microporosity grids and macropores; and (e2) the zoom-in view of the interface between pore *i*, microporosity grids *k* and *m*.

TABLE I. Pore-structure information of the three digital rocks of OM used in this work.

Pore-structure information	Three digital rocks of OM			
	OM-HP	OM-MP	OM-LP	
Morphology	Filamentous	Bubble-like	Sponge-like	
Connectivity of macropores along the Z direction	Interconnected	Isolated	Isolated	
Mean coordination number of macropores (full)	1.41	0.36	0.12	
Mean pore diameter of macropores (nm)	135.4 nm	107.8 nm	74.8 nm	
Porosity of macropores	23.9%	9.0%	7.7%	
Volume fraction of solid	1.7%	18.2%	0.05%	
Revised porosity of macropores ^a	24.3%	11%	8.1%	
The number of computational grids: macropores/microporosity grids	752/27 882	562/21 220	1436/26 028	

^aThe revised porosity of macropores here is defined as $\delta^p/(1-\nu^s)$, where δ^p is the porosity of macropores and ν^s is the volume fraction of solid.

OM macropores are interconnected along the Z direction, but not for the other two cores. It is worth noting that the three OM digital rocks are relatively homogeneous in terms of permeability and the connectivity of macropores. Therefore, in this work, we focus on shale gas

flow dynamics along the Z direction. Due to the high porosity of macropores in the digital rock of OM-HP, it has the largest coordination number of macropores of 1.41, which is much larger than the values (0.36 and 0.12) of the other two cores. This indicates that macropores

in the digital rocks of OM-MP and OM-LP have very poor connectivity, and OM microporosity may play a dominant role in regulating gas flow. Figure 3 shows the distributions of pore sizes and coordination numbers of macropores in the three OM digital rocks. It is seen that in comparison with the digital rocks of OM-HP and OM-MP, the digital rock of OM-LP has the most isolated small macropores and the lowest porosity of macropores (7.7%).

B. Governing equations of the pore-network-continuum model

In this subsection, we briefly present the governing equations of the pore-network-continuum model for nonlinear gas flow in OM. For the detail, one can refer to (Zhang et al., 2024). A digital rock of OM includes resolved macropores and sub-resolution microporosity. In the OM microporosity, flow and transport are described at the continuum scale and the mass conservation of methane gas is given as

$$\frac{\partial}{\partial t} \left[\left(\phi - \frac{n_{ad}}{\rho^{ad}} \right) \rho^{g} \right] + \frac{\partial n_{ad}}{\partial t} + \nabla \cdot \left(\rho^{g} \mathbf{q}^{g} \right) + \nabla \cdot \left(\rho^{ad} \mathbf{v}^{ad} \right) = 0, \quad (1)$$

where φ (-) is the porosity of microporosity regions; ρ^g (kg/m³) denotes the mass density of free methane; ρ^{ad} is the mass density of adsorbed methane, which is assumed to be constant; \mathbf{q}^g (m/s) is the Darcy velocity; \mathbf{v}^{ad} (m/s) is the surface diffusive velocity; and n_{ad} is the mass of adsorbed methane per unit volume of microporosity. The real gas equation of state is used to calculate the methane density by $\rho^g = Mp/ZRT$, where Z (-) is the gas compressibility factor by solving the Peng–Robinson equation (presented in Appendix A) (Peng and Robinson, 1976), p (Pa) is the gas pressure, R (J/kg/mol) is the universal gas constant, T (K) is the gas temperature, and M (kg/mol) is the molecular weight of methane.

Neglecting the gravity, the Darcy velocity with the consideration of gaseous slippage effect is given as

$$\mathbf{q}^{g} = -\text{fun}(Kn) \frac{k_{m}}{\mu} \nabla p, \tag{2}$$

where k_m (m²) is the intrinsic permeability of OM microporosity, μ is the dynamic viscosity estimated by the empirical formulas proposed by Lee *et al.* (1966) (presented in Appendix B), and fun(Kn) is a correction function of the Knudsen number for slippage effect. The Knudsen number is

defined as $Kn = \lambda/L$, where λ is the mean free path of methane estimated by $\lambda = (\mu/p)\sqrt{\pi ZRT/2M}$, and L is a characteristic length such as the mean pore diameter in microporosity. The high-resolution HIM images show that OM has mostly circular pores and throats (Wu *et al.*, 2017). Therefore, assuming OM microporosity to be a bundle of circular nano tubes, the correction function has the following form:

$$fun(Kn) = (1 + \alpha Kn) \left(1 + \frac{4Kn}{1 + Kn}\right), \tag{3}$$

where α is the fitting parameter given by $\alpha = 1.358$ $\times \frac{2}{\pi} tan^{-1} (4.0 Kn^{0.4})$ (Beskok and Karniadakis, 1999).

The surface diffusive velocity of absorbed methane is given as (Heller and Zoback, 2014)

$$\mathbf{v}^{ad} = -\frac{1}{\rho^{ad}} D_s \nabla n_{ad}, \tag{4}$$

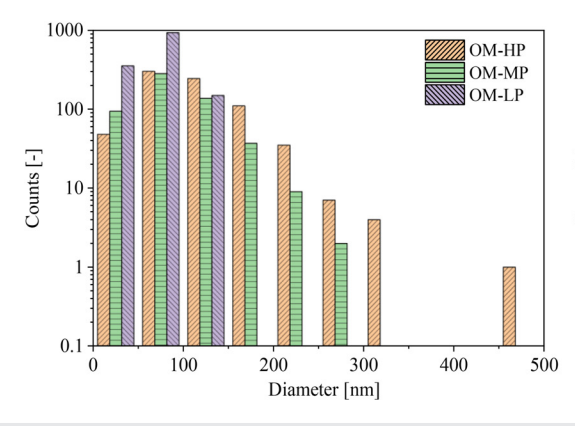
where D_s (m²/s) is the surface diffusivity. The mass of adsorbed methane per unit volume of microporosity is calculated as

$$n_{ad} = \frac{n_{ad}^{\text{max}} Kp}{1 + Kp},\tag{5}$$

where $n_{ad}^{\rm max}$ (kg/m³) is the maximum adsorption amount per unit volume of microporosity, and K (1/Pa) is the Langmuir coefficient, defined as the reciprocal of the pressure when half of the adsorption sites are occupied. In the OM microporosity, the adsorbed methane occupies part of the pore volume, which reduces the porosity of microporosity regions. As given in Eq. (1), the effective porosity of microporosity regions is $\varphi - \frac{n_{ad}}{\rho^{ad}}$, where $\frac{n_{ad}}{\rho^{ad}}$ is the porosity occupied by adsorbed gas. Therefore, with the increase in gas pressure, the mass of free methane per unit volume of microporosity, $\left(\varphi - \frac{n_{ad}}{\rho^{ad}}\right) \rho^{\rm g}$, will reach the maximum, and then decrease slightly, as shown in Fig. 4.

Given the fact that the pore sizes of macropores are much larger than those in microporosity (see Table I), adsorption and surface diffusion in macropores can be neglected. In the hybrid pore-network-continuum modeling framework, flow and transport in macropores are described by a pore-network model given by Shi et al. (2024),

$$V_i \frac{\partial \rho_i^g}{\partial t} + \sum_{j=1}^{N_i} \rho_j^g \max\left(Q_{ij}^g, 0\right) + \sum_{j=1}^{N_i} \rho_j^g \min\left(Q_{ij}^g, 0\right) = 0, \quad (6)$$



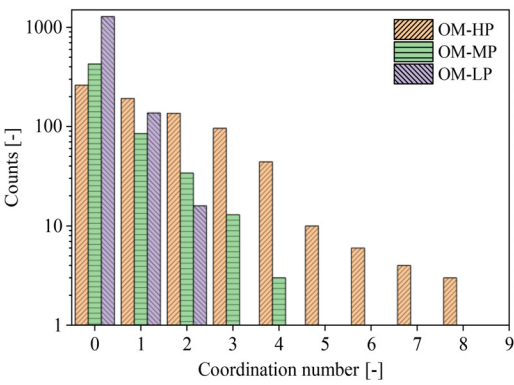


FIG. 3. The distribution of pore sizes and coordination numbers of macropores in the three OM digital rocks

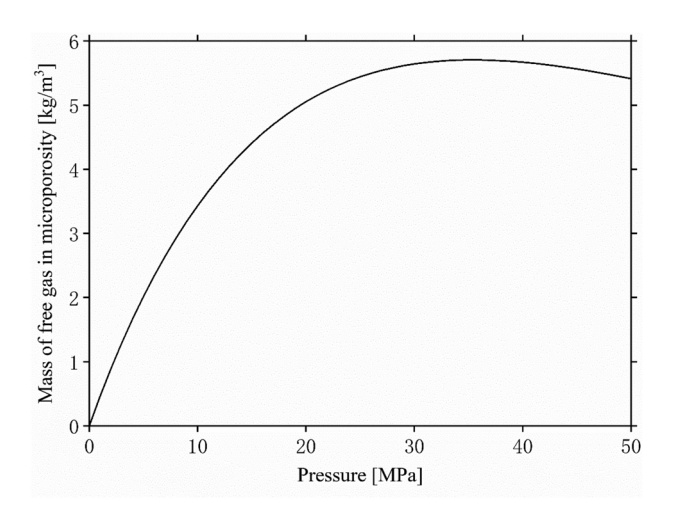


FIG. 4. Mass of free gas (i.e., excluding adsorbed gas) per unit volume of microporosity as a function of gas pressure. The initial porosity of microporosity regions is 10%, and the real gas equation of state was used.

where V_i (m³) is the volume of pore body i, N_i is the coordination number of pore body i, and Q_{ij}^g (m³/s) is the volumetric flux of methane given by $Q_{ij}^g = T_{ij} \left(p_i^g - p_j^p \right)$, where T_{ij} is the transmissibility between the two pore bodies including the slippage effect.

By assuming an isothermal condition, Eqs. (1) and (6) are the basic governing equations of mass conservation of methane in both microporosity and macropores, which are complemented by the flow equations (2) and (4). The primary unknown variable is gas pressure in microporosity and macropores. The secondary variables such as gas density, apparent permeability, and mass of adsorbed methane are dependent on gas pressure.

C. Numerical implementation and verification

By the implicit Euler scheme, the upwind finite volume scheme, and the two-point flux approximation scheme (TPFAS), Eq. (1) can be discretized as

$$\frac{MV_{i}\varphi}{RT\Delta t} \left(\frac{p_{i}^{t+\Delta t}}{Z_{i}^{t+\Delta t}} - \frac{p_{j}^{t}}{Z_{i}^{t}} \right) + \frac{n_{ad}^{\max}V_{i}}{\Delta t} \left[\left(1 - \frac{Mp_{i}^{t+\Delta t}}{Z_{i}^{t+\Delta t}RT\rho^{ad}} \right) \right] \\
\times \frac{Kp_{i}^{t+\Delta t}}{1 + Kp_{i}^{t+\Delta t}} - \left(1 - \frac{Mp_{i}^{t}}{Z_{i}^{t}RT\rho^{ad}} \right) \frac{Kp_{i}^{t}}{1 + Kp_{i}^{t}} \right] \\
+ \sum_{j=1}^{N_{i}} \frac{Mp_{i}^{t+\Delta t}}{Z_{i}^{t+\Delta t}RT} \max \left(T_{ij}^{t+\Delta t} \left(p_{i}^{t+\Delta t} - p_{j}^{t+\Delta t} \right), 0 \right) \\
+ \sum_{j=1}^{N_{i}} \frac{Mp_{j}^{t+\Delta t}}{Z_{j}^{t+\Delta t}RT} \min \left(T_{ij}^{t+\Delta t} \left(p_{i}^{t+\Delta t} - p_{j}^{t+\Delta t} \right), 0 \right) \\
+ \sum_{i=1}^{N_{i}} T_{ij}^{ad,t+\Delta t} \left(p_{i}^{t+\Delta t} - p_{j}^{t+\Delta t} \right) = 0, \tag{7}$$

where V_i is the grid volume, N_i is the number of shared faces with microporosity grid i, $T_{ii}^{t+\Delta t}$ is the transmissibility for Darcy flux, and

 $T^{ad,t+\Delta t}_{ij}$ is the transmissibility for surface diffusion. According to Eq. (2) and the harmonic average, $T^{t+\Delta t}_{ij}$ can be given as

$$T_{ij}^{t+\Delta t} = \frac{a_i a_j}{a_i + a_j}, \quad \text{with} \quad a_i = \text{fun}(Kn_i) \frac{k_i A_i}{\mu d_i} \mathbf{n}_i \cdot \mathbf{f}_i$$

and

$$a_j = \operatorname{fun}(\operatorname{Kn}_j) \frac{k_j A_j}{\mu d_i} \mathbf{n}_j \cdot \mathbf{f}_j, \tag{8}$$

where a_i and a_j are the transmissibility of microporosity grids i and j, respectively; A_i is the interfacial area between the two grids; d_i is the distance between the centroid of the interface and the centroid of grid i; Kn_i is the Knudsen number in grid i; \mathbf{n}_i is the unit normal to the interface inside grid i; and \mathbf{f}_i is the unit along the direction of the line joining the grid centroid to the centroid of the interface. According to Eq. (4) and the harmonic average, $T_{ii}^{ad,t+\Delta t}$ can be given as

$$T_{ij}^{ad,t+\Delta t} = \frac{a_i^{ad} a_j^{ad}}{a_i^{ad} + a_i^{ad}}, \quad \text{with} \quad a_i^{ad} = \frac{A_i D_s n_{ad}^{\max} K}{\left(1 + K p_i^{t+\Delta t}\right)^2 d_i} \mathbf{n}_i \cdot \mathbf{f}_i$$

and

$$a_j^{ad} = \frac{A_j D_s n_{ad}^{\text{max}} K}{\left(1 + K p_i^{t + \Delta t}\right)^2 d_i} \mathbf{n}_j \cdot \mathbf{f}_j. \tag{9}$$

By the implicit Euler scheme, Eq. (6) can be discretized as

$$\frac{MV_{i}\varphi}{RT\Delta t} \left(\frac{p_{i}^{t+\Delta t}}{Z_{i}^{t+\Delta t}} - \frac{p_{j}^{t}}{Z_{i}^{t}} \right)
+ \sum_{j=1}^{N_{i}} \frac{Mp_{i}^{t+\Delta t}}{Z_{i}^{t+\Delta t}RT} \max \left(T_{ij}^{t+\Delta t} \left(p_{i}^{t+\Delta t} - p_{j}^{t+\Delta t} \right), 0 \right)
+ \sum_{j=1}^{N_{i}} \frac{Mp_{j}^{t+\Delta t}}{Z_{i}^{t+\Delta t}RT} \min \left(T_{ij}^{t+\Delta t} \left(p_{i}^{t+\Delta t} - p_{j}^{t+\Delta t} \right), 0 \right) = 0.$$
(10)

The difference from Eq. (7) is that in Eq. (10), i and j denote the two neighboring pore bodies, and N_i is the coordination number of pore body i. Furthermore, the transmissibility, $T_{ij}^{t+\Delta t}$, is given as

$$T_{ij}^{t+\Delta t} = \frac{\operatorname{fun}(\operatorname{Kn}_{i}) + \operatorname{fun}(\operatorname{Kn}_{j})}{2} \frac{\pi R_{ij}^{4}}{8\mu l_{ii}}, \tag{11}$$

where R_{ij} is the equivalent radius of pore throat ij, l_{ij} is the pore throat length.

At the interface of microporosity and macropores, we impose the condition of mass-flux and pressure continuities. The mass flux across the interface between pore body i and microporosity control volume j is given as

$$\dot{m} = \frac{Mp_i^{t+\Delta t}}{Z_i^{t+\Delta t}RT} \max \left(T_{ij}^{t+\Delta t} \left(p_i^{t+\Delta t} - p_j^{t+\Delta t} \right), 0 \right) + \frac{Mp_j^{t+\Delta t}}{Z_i^{t+\Delta t}RT} \min \left(T_{ij}^{t+\Delta t} \left(p_i^{t+\Delta t} - p_j^{t+\Delta t} \right), 0 \right), \tag{12}$$

where $T_{ij}^{t+\Delta t}$ is the total transmissibility given as

$$\begin{split} T_{ij}^{t+t} &= \frac{a_i a_j}{a_i + a_j}, \quad \text{with} \quad a_i = \text{fun}(\mathbf{K}\mathbf{n}_i) \frac{\pi R_i^{\ 4}}{8\mu l_i} \\ \text{and} \\ a_j &= \left(\text{fun}(\mathbf{K}\mathbf{n}_j) \frac{k_j A_j}{\mu d_j} + \frac{A_j D_s n_{ad}^{max} K}{\rho_i^{t^*} \left(1 + K p_j^{t+\Delta t} \right)^2 d_j} \right) \mathbf{n}_j \cdot \mathbf{f}_j p_i^{t+\Delta t} > p_j^{t+\Delta t} \\ &\times \left(\text{fun}(\mathbf{K}\mathbf{n}_j) \frac{k_j A_j}{\mu d_j} + \frac{A_j D_s n_{ad}^{max} K}{\rho_j^{t^*} \left(1 + K p_j^{t+\Delta t} \right)^2 d_j} \right) \mathbf{n}_j \cdot \mathbf{f}_j p_i^{t+\Delta t} < p_j^{t+\Delta t}, \end{split}$$

(13

where l_i is assumed to be equal to R_i (i.e., the equivalent radius of pore body i).

With Eq. (12), we can couple Eqs. (7) and (10) together. Then, the only unknown variable is methane pressure in OM macropores and microporosity. Due to the consideration of real gas EOS, methane compressibility, slippage effect, and surface diffusion, the resultant algebraic equations are highly nonlinear. The Newton-Raphson method is used with a relative residual of 10⁻⁶. The GPU-parallel FGMRES (Flexible Generalized Minimal Residual method) solver is used for linearized algebraic equations. The present pore-network-continuum model for shale gas flow has been implemented based on an in-house simulator programed by C++. The numerical verification against direct numerical simulations can be found in our previous work of Shi et al. (2024); Zhang et al. (2024), which will not be repeated here. Finally, Table II lists the constant parameters used in our numerical simulations (Rexer et al., 2014). The surface diffusion coefficient is mainly dependent on methane pressure; in this work, we take typical values from Medved et al. (2011) as shown in Table III, which is mainly pressure-dependent.

III. RESULTS AND DISCUSSION

The pore-network-continuum model presented in Sec. III will be used to study transient processes of shale gas production from OM. By dropping the transient terms of governing equations (1) and (6), we can simulate steady-state nonlinear gas flow and predict the apparent

TABLE II. Constant parameters used in our numerical simulations.

Parameters	Values
Langmuir coefficient (K)	$4 \times 10^{-8} 1/Pa$
Maximum adsorption (n_{max}^{ad})	44.8kg/m^3
Density of adsorbed methane (ρ_{ad})	$400 \mathrm{kg/m^3}$
Temperature	400 K
Characteristic length of microporosity, L	6.96 nm
Intrinsic permeability of OM microporosity	12.3 nD

TABLE III. Surface diffusion coefficient as a function of gas pressure.

Gas pressure (MPa)	1	5	10	20	30	40	50
$D_s (10^{-8} \mathrm{m}^2/\mathrm{s})$	8.32×10^{-1}	9.52×10^{-1}	1.14	1.44	1.77	2.10	2.46

permeability of OM. If we further neglect the nonlinear flow processes including adsorption, slippage effect, and surface diffusion, the intrinsic permeability of OM can be predicted. In Sec. III A, we will discuss the intrinsic and apparent permeability of the three types of OM, which is followed by transient simulations of shale gas production in OM under different reservoir pressures in Sec. III B. In Sec. III C, we present an empirical equation for OM apparent permeability.

A. Intrinsic and apparent permeability of organic matter

We first present the intrinsic permeability of OM, which is purely determined by the characteristic of pore structures. Along the flow direction, we impose a pressure drop of 100 Pa. The remaining boundaries are set to no flow. Once the pressure field is obtained, we can use the Darcy equation to calculate the intrinsic permeability. From this point onward, the digital rocks of OM-HP, OM-MP, and OM-LP will be referred to simply as OM-HP, OM-MP, and OM-LP, respectively, for the sake of brevity. The intrinsic permeability of OM-HP, OM-MP, and OM-LP is numerically predicted to be 1095, 14.9, and 14.8 nD, respectively $(1 \text{ nD} \approx 10^{-21} \text{ m}^2)$. OM-HP has two orders of magnitude larger intrinsic permeability than the other two. By recalling the analysis of OM pore structures in Table I, this is because OM-HP has interconnected pathways of macropores throughout the domain. Moreover, it is seen that the intrinsic permeability of OM-MP and OM-LP is very close to the intrinsic permeability of OM microporosity (12.3 nD in Table II). This indicates that most macropores of OM-MP and OM-LP are isolated and the porosity of macropores should be low. This can be confirmed by the coordination numbers (much smaller than unity) and the porosity (below 10%) of macropores listed in Table I. Therefore, flow in the macropores of OM-MP and OM-LP must be facilitated by the OM microporosity.

Figure 5 shows the volumetric flux and pressure distributions in the three digital rocks of OM by the modeling of intrinsic permeability. For each OM, the fluxes lower than 10% of its maximum are transparentized for better illustration. The first column shows the flux distributions in the OM macropores, where the colormap range is normalized by the maximum flux in each OM. It is seen that OM-HP has two preferential flow pathways of interconnected macropores with high fluxes, while the remaining macropores are either isolated or locally connected. The fluxes in the macropores of OM-MP and OM-LP are much smaller, and the majority of macropores are isolated. The second column shows the fluxes in the OM microporosity. Still, the fluxes lower than 10% of maximum are transparentized for better illustration and the colormap ranges are normalized by the maximum fluxes in the microporosity. OM-HP and OM-MP show some relatively high flux regions, which play a role in connecting surrounding macropores for gas flow. However, OM-LP does not show this tendency, because almost all macropores in OM-LP are isolated and do not form local clusters. The homogeneous OM microporosity controls even gas flow in the domain. It is worth noting that OM microporosity can be heterogenous, and its impact on gas flow will be a future study. The third column shows the steady-state pressure distributions, which is relative to a background reservoir pressure value. When linear gas flow and absence of adsorption are assumed here, the background pressure will not influence the prediction of intrinsic permeability. It is seen that the pathways of interconnected macropores in OM-HP dramatically impact the pressure field, which will play a role in the gas production

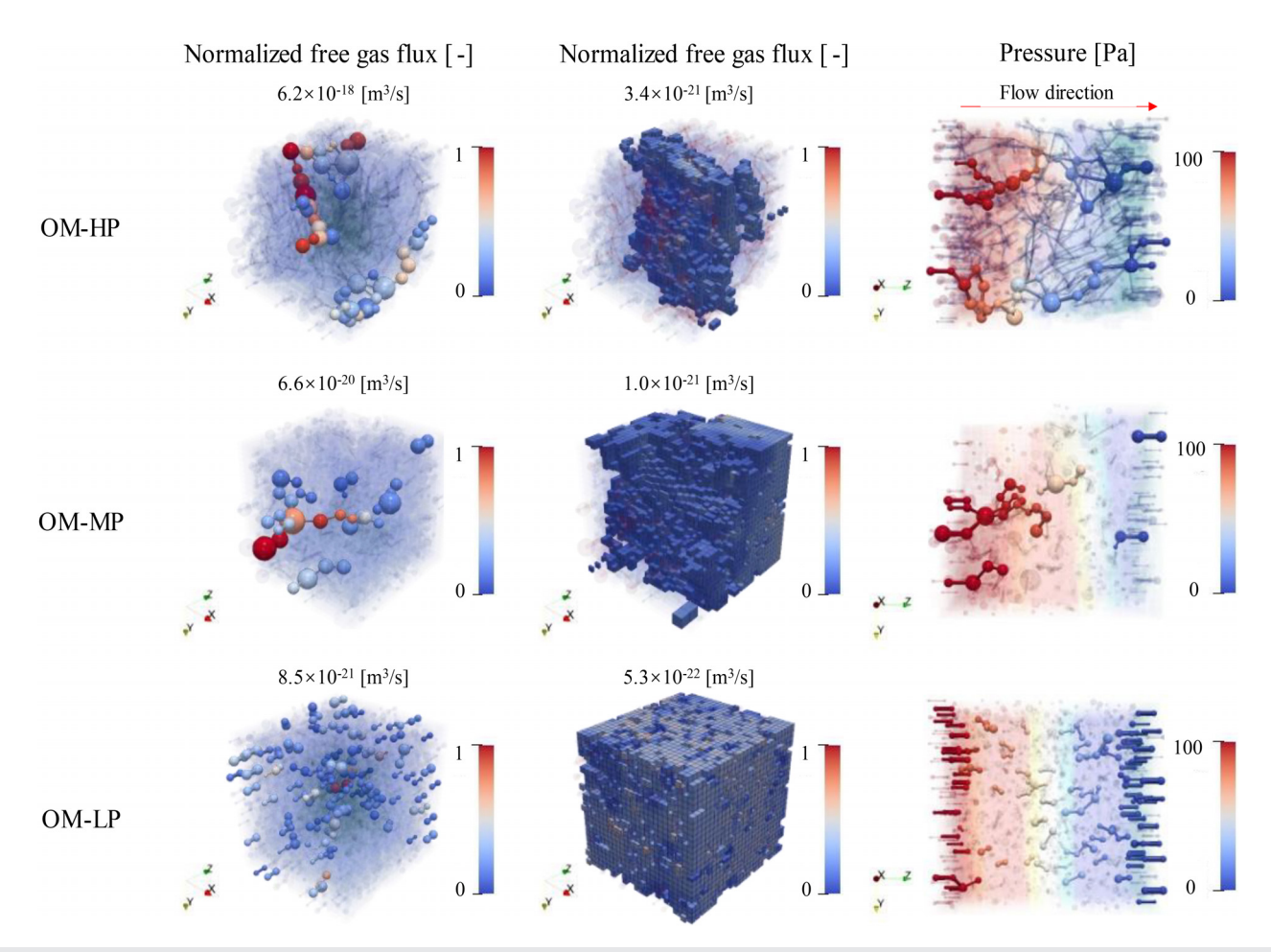


FIG. 5. Normalized volumetric flux and pressure distributions in the three digital rocks of OM by the modeling of intrinsic permeability (i.e., steady state and linear process are considered). The first and second columns display volumetric flux distributions in the macropores and microporosity, respectively. The fluxes lower than 10% of maximum are transparentized for better illustration. (The maximum volumetric flux in macropores is given on the top of each graph in the first column, and the maximum volumetric flux in microporosity is given on the top of each graph in the second column.) The third column shows the steady-state pressure (relative to the background reservoir pressure) distributions.

process (later see Sec. IV B). OM-MP has some local connected macropores, which slightly impact the pressure field. Finally, OM-LP shows uniform and gradual pressure drop along the flow direction, because the homogeneous OM microporosity controls even gas flow as mentioned above.

Regarding shale gas production, we are more interested in apparent permeability of OM. Both slippage effect in OM and surface diffusion in microporosity will enhance gas flow and make apparent permeability much larger than intrinsic permeability. It is also known that slippage flow and surface diffusion reduce as the increase in shale gas pressure [see Eqs. (2) and (4)]. In this work, we numerically predict apparent permeability under a wide range of reservoir gas pressures and investigate its pressure dependence. Figure 6(a) shows the apparent permeability of the three digital rocks of OM under different gas pressures from 1 to 50 MPa. As expected, the apparent permeability first decreases dramatically and then gradually approaches to the intrinsic permeability. Figure 6(b) shows the apparent permeability of OM microporosity and the comparison with the apparent permeability

of OM-MP and OM-LP. For microporosity itself, the intrinsic permeability is 12.3 nD. At 1 MPa, the apparent permeability with and without surface diffusion is 140 and 96.7 nD, respectively. It indicates that for gas flow in microporosity, slippage effect will be more important than surface diffusion. By calculation, it is found that slippage effect and surface diffusion contribute to about 60% and 31% of the apparent permeability, respectively. This conclusion will also apply to OM-MP and OM-LP, because microporosity of OM-MP and OM-LP controls gas flow in OM as discussed above.

Table IV lists the ratios of apparent permeability to intrinsic permeability at the reservoir pressures of 1 and 50 MPa for the three digital rocks of OM. It is seen that at the low pressure of 1 MPa, the apparent permeability of OM-MP and OM-LP is around ten times larger than the intrinsic permeability, which is also the case for microporosity. However, OM-HP has a much smaller ratio of 2.35. Although slippage effect and surface diffusion considerably enhance gas flow in OM-HP microporosity, slippage flow in interconnected macropores dominates the apparent permeability. Moreover, given the

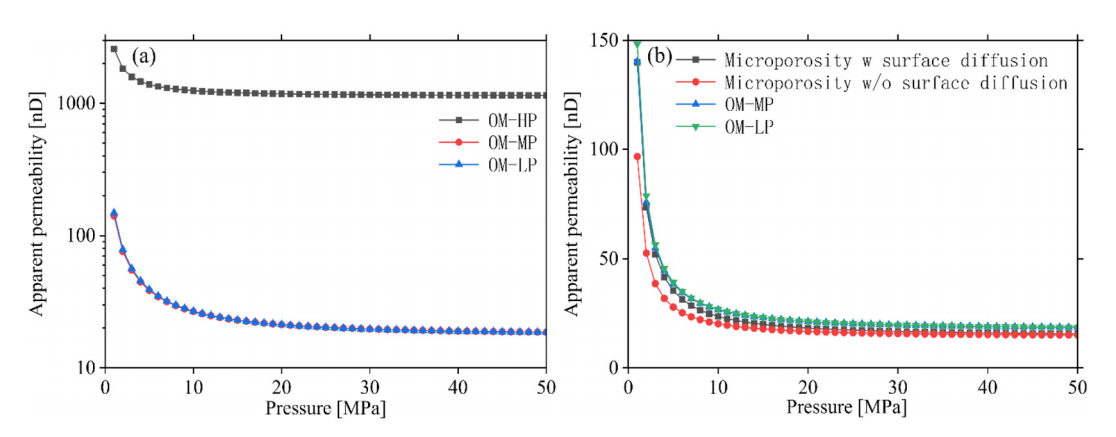


FIG. 6. (a) Apparent permeability of the three digital rocks of OM vs shale gas pressure and (b) apparent permeability of microporosity and the comparison with OM-MP and OM-LP vs shale gas pressure.

much larger pore sizes of macropores, the value of the correction function of the Knudsen number for slippage effect [refer to Eq. (3)] is much smaller than that for microporosity. Although slippage effect in OM-HP is not as strong as those in OM-MP and OM-LP, the apparent permeability of OM-HP is still much larger than the other two OM as shown in Fig. 6(a). This is because the intrinsic permeability of OM-HP is much larger (1095 nD).

To sum up, first, we show that both intrinsic permeability and apparent permeability are strongly dependent on pore structures of OM. In this work, OM-HP has high porosity (24.3%) and interconnected macropores throughout the domain. As a result, it has the highest intrinsic permeability of 1095 nD. However, at the low reservoir pressure of 1 MPa, the apparent permeability of OM-HP is only 2.35 times higher than its intrinsic permeability, because slippage effect in the interconnected macropores dominates gas flow. In contract, OM-MP and OM-LP have relatively low porosity and no pathways of connected macropores are formed, where OM microporosity controls gas flow. As a result, OM-MP and OM-LP have much smaller intrinsic permeability that is very close to the OM intrinsic permeability of 12.3 nD. However, at the low reservoir pressure of 1 MPa, the apparent permeability of OM-MP and OM-LP is about ten times higher than their intrinsic permeability, because slippage effect and surface diffusion in OM microporosity are much pronounced. Overall, OM-HP still has much higher apparent permeability than OM-MP and OM-LP. Second, in our case studies, we show that in OM microporosity, slippage effect is more important than surface diffusion, which is

TABLE IV. The ratios of apparent permeability to intrinsic permeability at the reservoir pressures of 1 and 50 MPa for the three digital rocks of OM.

The ratios of apparent to

	intrinsic permeability $(k_{a,om}/k_{om})$		
Digital rocks	At 1 MPa	At 50 MPa	
OM-HP	2.35	1.05	
OM-MP	9.42	1.24	
OM-LP	10.01	1.25	
Microporosity	11.37	1.27	

opposite to the conclusion given in the work of Guo *et al.* (2018). This is because the OM microporosity has much larger intrinsic permeability (12.3 nD) than that (0.69 nD) used in Guo *et al.* (2018). As a key material property of OM, its determination is crucial to our quantitative understanding of gas flow capacity in shale. Last, our case studies indicate that the classification of OM units will be crucial to the upscaling study of shale gas flow. Moreover, OM porosity may be an important and convenient parameter to the classification, because morphology and connectivity of OM macropores have strong correlation with porosity.

B. Transient simulations of shale gas production in organic matter

Shale gas production and gas occurrence states strongly depend on the gas reservoir pressure. The real gas production can last a few years. For simplicity, to study shale gas production dynamics, we use a low reservoir pressure of 5 MPa and a high reservoir pressure of 50 MPa as the background pressures, corresponding to a late and an early stages of gas production. In our case studies, we impose a pressure drop of 100 Pa along the Z direction, i.e., we set the Dirichlet boundary condition of 0 Pa pressure (relative to the background reservoir pressure) at the Z max, the remaining are imposed of the no-flux boundary condition. Initially, we set a relative pressure of 100 Pa in the domain.

Table V lists the total amounts of gas production at the two reservoir pressures of 5 and 50 MPa. The pressure drop is set to $100 \, \text{Pa}$ in our case studies. It is seen that at 5 MPa OM-HP has slightly more gas

TABLE V. The total amounts of gas production at the two different reservoir pressures with a pressure drop of 100 Pa.

	Gas production	Gas production amount (g)		
Digital rocks	At 5 MPa	At 50 MPa		
OM-HP	1.16×10^{-18}	3.29×10^{-19}		
OM-MP	8.54×10^{-19}	1.54×10^{-19}		
OM-LP	1.01×10^{-18}	1.52×10^{-19}		

production than those of OM-MP and OM-LP, because the porosity of macropores in OM-HP is higher. The macropores of OM-HP can contain more free gas. At 50 MPa, free gas in the macropores will dominate gas production of all the three OM. As a result, OM-HP with a high porosity has twice more gas production than those of OM-MP and OM-LP. It is also seen that for each type of OM, the total amount of gas production at 5 MPa is much larger than that at 50 MPa, which can be justified by much more adsorption in microporosity at 5 MPa and the real gas equation of state.

Figure 7 shows the dimensionless cumulative gas production curves of the three digital rocks of OM, at the low reservoir pressure of 5 MPa and the high reservoir pressure of 50 MPa. The dimensionless production time is defined by $T^* = t/T_D$, where t is the physical production time and T_D is the reference time. The reference time (i.e., the surface diffusion time) is calculated by $T_D = L^2/D_s$, where L is the domain length (1.6 μ m) and D_s is the surface diffusion $(9.52 \times 10^{-9} \,\mathrm{m}^2/\mathrm{s})$ in OM microporosity at 5 MPa. The reference gas production is the total amount of gas production of each case given in Table V. As shown in Figs. 8(a) and 8(d), at the low reservoir pressure of 5 MPa, gas production of OM-HP from the macropores is comparable to free gas and adsorbed gas in the microporosity due to its high porosity. However, at the high reservoir pressure of 50 MPa, free gas production in the macropores is dominant accounting for about 80% of the total gas production, mainly due to the high methane density (213.6 kg/m³). In contrast, at the low reservoir pressure of 5 MPa, adsorbed gas production in the microporosity is much larger than free gas production in the macropores for either OM-MP or OM-LP, due to the low porosity [Figs. 7(b) and 7(c)]. At the high reservoir pressure of 50 MPa, free gas in the macropores is the first source of gas production, accounting for more than half of the total gas production [Figs. 7(e) and 7(f)]. To sum up, at high reservoir pressures free gas in OM macropores is the major source of gas production. At low reservoir pressures, absorbed gas in OM microporosity dominates the gas production, expect for high-porosity OM (e.g., OM-HP) where free gas in macropores can be comparable to adsorbed gas in microporosity. Finally, it is worth noting that the negative production of free gas in microporosity at the high reservoir pressure of 50 MPa is due to the fact that with the increase in gas pressure, the mass of free gas per unit volume of microporosity, $\left(\varphi - \frac{n_{ad}}{\rho^{ad}}\right)\rho^g$, will reach the maximum, and then decrease slightly, as shown in Fig. 4. Therefore, des-

orbed gas production can leave more free gas in the OM microporosity than before the exploitation.

In Fig. 7, we can further observe the dynamics of gas production. It is seen that the gas production time of OM-HP is much shorter than those of OM-MP and OM-LP. This is because the connected macropores in OM-HP can efficiently transport adsorbed gas in the OM microporosity. Also, we observe that free gas production in the macropores is much faster than gas production in the microporosity at both low and high reservoir pressures. As mentioned before, the macropores of OM-MP and OM-LP are mostly isolated or locally clustered, which are connected by the OM microporosity. As a result, the OM microporosity controls gas flow. Free gas in the macropores and adsorbed gas in the microporosity flow out of the domain together, and there is no time-separation of the two gas production processes. Finally, Fig. 8 shows the pressure distributions (relative to the reservoir pressure of 1 MPa) in the three digital rocks of OM at

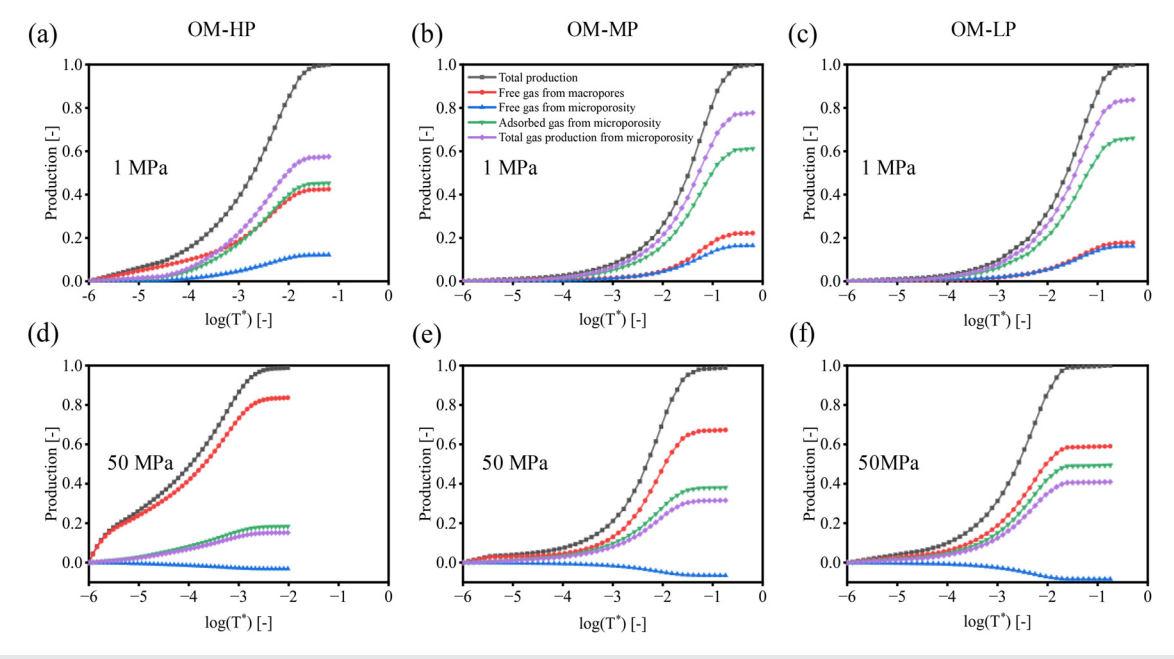


FIG. 7. Dimensionless cumulative gas production curves of the three digital rocks of OM, at the low reservoir pressure of 5 MPa and the high reservoir pressure of 50 MPa. In each case, there are five curves including total production, free gas from macropores, free gas from OM microporosity, adsorbed gas from OM microporosity, and total gas production from OM microporosity. The dimensionless production time is defined by $T^* = t/T_D$, where t is the physical production time, and T_D is the reference time. The reference ence time (i.e., the surface diffusion time) is calculated by $T_D = L^2/D_s$, where L is the domain length and D_s is the surface diffusion in OM microporosity at 5 MPa. The reference gas production is the total amount of gas production of each case given in Table V.

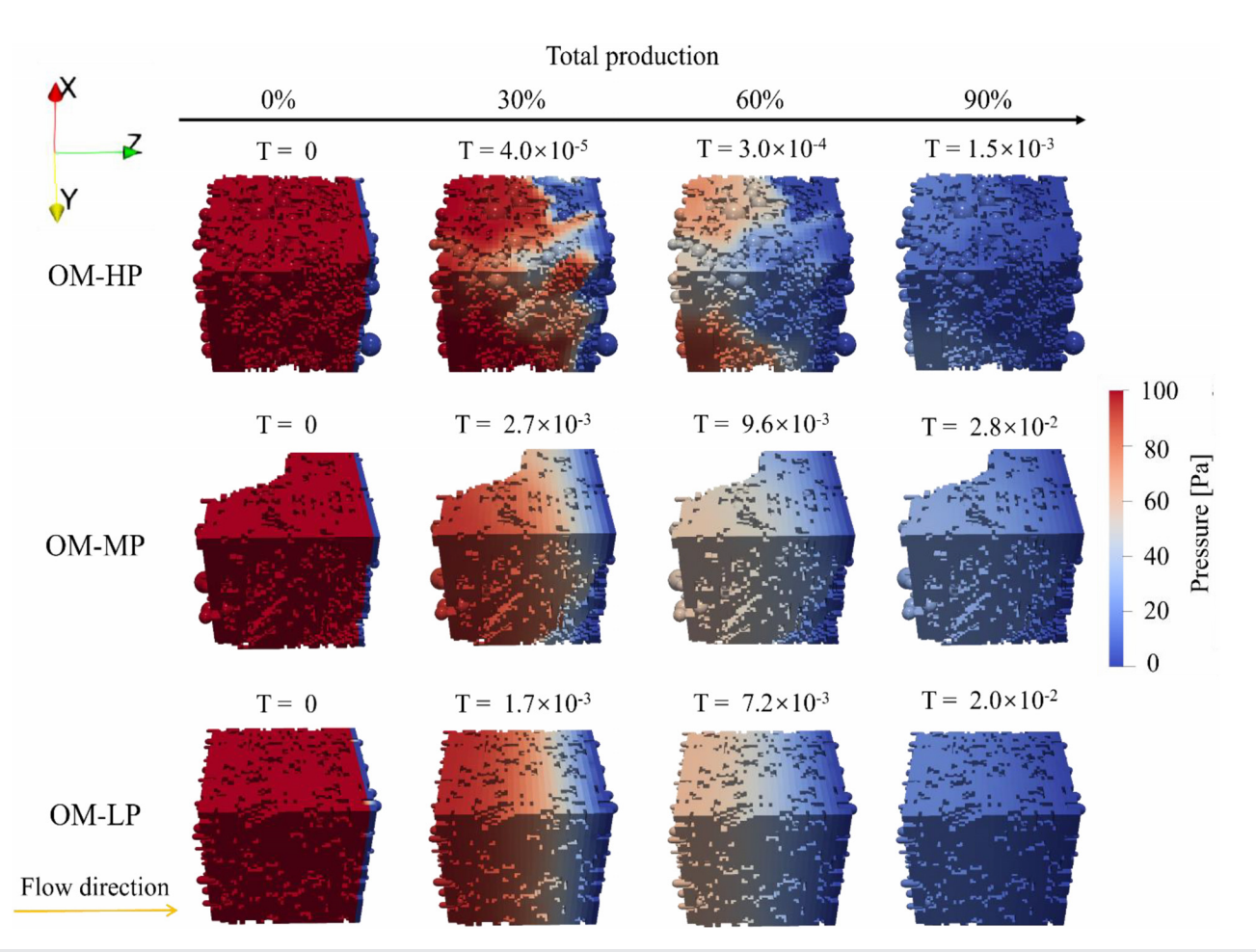


FIG. 8. Pressure distributions (relative to the reservoir pressure of 5 MPa) in the three digital rocks of OM at the total dimensionless gas production of 0%, 30%, 60%, and 90%. The dimensionless production time is defined by $T^* = t/T_D$, where t is the physical production time, and T_D is the reference time. The reference time (i.e., the surface diffusion time) is calculated by $T_D = L^2/D_s$, where L is the domain length and D_s is the surface diffusion in OM microporosity at 5 MPa. The reference gas production is the total amount of gas production of each case given in Table V.

the total dimensionless gas production of 0%, 30%, 60%, and 90%. It is seen that in OM-HP, the decline of gas pressure follows the connected macropores, while in either OM-MP or OM-LP, the decline of gas pressure gradually and homogenously penetrates to the left side of the domain. This observation is in consistent with the production curves in Fig. 7.

C. Empirical formula for apparent permeability of organic matter

Extensive work has been conducted to model the apparent permeability of OM, coupling multiple physical mechanisms and the dynamic deformation of OM pores (Sheng et al., 2019; 2020; Tian et al., 2023; and Wang et al., 2022). However, due to the lack of investigation into 3D pore structures of OM, those studies neglect interconnected macropores within OM. As a result, empirical formulas for apparent permeability of OM are still missing. As a first attempt, we propose a simple but accurate formula for calculating the apparent

permeability of OM. By adding free gas flux with slippage effect and surface diffusion flux of adsorbed gas, the following formula of apparent permeability can be derived (Guo *et al.*, 2018):

$$k_{a,om} = -\left(\mathbf{q}^{g} + \mathbf{v}^{ad} \frac{\rho^{ad}}{\rho^{g}}\right) \mu / \nabla p$$

$$= \frac{1}{\rho^{g}} \mu D_{s} n_{ad}^{\max} \frac{K}{\left(1 + Kp\right)^{2}} + \left(1 + \alpha \bar{K}n\right) \left(1 + \frac{4\bar{K}n}{1 + \bar{K}n}\right) k_{om},$$
(14)

where $k_{a,om}$ is the apparent permeability of OM, k_{om} is the intrinsic permeability, and $\bar{K}n$ is the average Knudsen number of OM defined as $\bar{K}n = \lambda/L^{eff}$ where L^{eff} is the effective characteristic length of OM. Notice that in Eq. (13), the pressure-dependent surface diffusion coefficient, D_s , is given in Table III, and the gas density, ρ^g , is calculated by the real gas EOS. The effective characteristic length of OM is the only fitting parameter in the empirical formula.

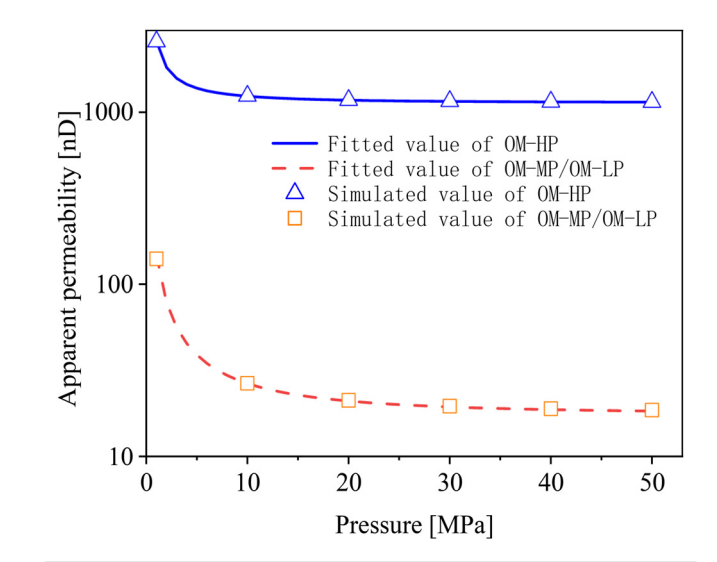


FIG. 9. Apparent permeability of OM-HP, OM-MP, and OM-LP vs reservoir pressure. The apparent permeability of OM-MP and OM-LP is almost overlapped, which is shown together here.

As shown in Fig. 9, the empirical formula with the fitted characteristic lengths can well reproduce the numerical results. The fitted characteristic lengths for OM-HP and OM-MP/OM-LP are 33 and 7.5 nm, respectively. It is found that the effective characteristic length for OM-HP is close to the minimum pore-throat diameter of macropores (36 nm). In contract, the effective characteristic length for OM-MP/ OM-LP is very close to the mean pore diameter of micropores in microporosity (6.96 nm given in Sec. II A). This is because microporosity dominates flow and transport in OM instead of isolated macropores.

IV. CONCLUSIONS

Organic matter (OM) is the main source of hydrocarbons in shales. Comprehensive understanding of its permeability and gas production characteristics is vital for accurately analyzing production curves of shale gas reservoirs and optimizing exploitation strategies. In this work, for the first time, we have developed an efficient pore-network-continuum model for nonlinear gas flow in digital rocks of OM. We select three types of OM mainly featured by their distinct porosities and morphologies. The digital rocks are constructed based on their FIB-SEM images and the information of low-temperature gas adsorption data, which compose of resolved OM macropores and subresolution OM microporosity. Based on a number of case studies under different reservoir pressures, we show that high-porosity OM (OM-HP in this work) may have interconnected macropores throughout the domain, which dominate the intrinsic permeability of OM. Furthermore, slippage effect of connected macropores dominates the apparent permeability. For low-porosity OM (OM-MP and OM-LP in this work), sub-resolution OM microporosity controls gas flow. As a result, the intrinsic permeability is close to the intrinsic permeability of microporosity. At low reservoir pressures (1 MPa in this work), slippage effect and surface diffusion in the microporosity dominate the apparent permeability which can be ten times larger than the intrinsic permeability. This is distinct from high-porosity OM.

Porous structures of OM also impact gas production and occurrence states. Free gas in macropores is the major source of gas production at a high reservoir pressure (e.g., 50 MPa, an early stage of exploitation). In a low reservoir pressure (e.g., 5 MPa), adsorbed gas in microporosity is dominant, expect for high-porosity OM where free gas in macropores is comparable to adsorbed gas in microporosity. Finally, there is time-separation of the two gas production processes (i.e., free gas production in macropores and adsorbed gas production in microporosity) for high-porosity OM, not for low-porosity OM. Also, gas production in high-porosity OM is much faster than low-porosity OM.

Our work has verified that OM can be distinct by the connectivity of its macropores, which may be indicated by its porosity, i.e., highporosity OM may have connected macropores. OM can have totally different intrinsic permeability, mechanisms of the apparent permeability, gas occurrence, and gas production processes. This indicates that the classification of OM can be crucial to the upscaling studies of gas flow. For instance, in the REV modeling of shale flow, OM cannot be directly homogenized or averaged. At least, the classification based on the OM porosity needs to be conducted. Based on our numerical results, an empirical formula for the apparent permeability of OM with distinct pore structures is proposed and can be directly used in the REV-scale modeling of gas flow in shale matrix. Finally, in the future study, we will release the assumption of homogenous microporosity and improve the computational performance to avoid the reduction of voxel resolution.

ACKNOWLEDGMENTS

We acknowledge the support of National Natural Science Foundation of China (Grant No. U23A20595), the Youth Science and Technology Project of CNPC (2024DQ0.037), and the Science and Technology Project of CNPC (No. 2023ZZ21). All data in this work is available upon request (chaozhong.qin@gmail.com).

AUTHOR DECLARATIONS Conflict of Interest

The authors have no conflicts to disclose.

Author Contributions

Dongchen Liu: Investigation (equal); Project administration (equal); Resources (equal); Supervision (equal); Writing - review & editing (equal). Xuefeng Yang: Formal analysis (equal); Investigation (equal); Resources (equal); Writing – original draft (equal). Deliang Zhang: Data curation (equal); Investigation (equal); Resources (equal). Shan Huang: Formal analysis (equal); Investigation (equal); Methodology (equal). Rui Jiang: Formal analysis (equal); Investigation (equal). Jianqi Rong: Formal analysis (equal); Investigation (equal); Software (equal); Validation (equal); Writing original draft (equal). Zhiwei Wang: Investigation (equal); Software (equal); Visualization (equal). Bowen Shi: Formal analysis (equal); Validation (equal). Chao-Zhong Qin: Conceptualization (equal); Funding acquisition (equal); Project administration (equal); Supervision (equal); Writing - review & editing (equal).

DATA AVAILABILITY

The data that support the findings of this study are available from the corresponding authors upon reasonable request.

APPENDIX A: EQUATION-OF-STATE AND VISCOSITY EQUATION FOR METHANE

We use the Peng–Robinson equation to describe the density of methane. First, reduced temperature T_r and reduced pressure P_r are given as

$$P_r = \frac{P}{P_c},\tag{A1}$$

$$T_r = \frac{T}{T_c},\tag{A2}$$

where P_c is the critical pressure of methane and equals to 4.599 MPa, T_c is the critical temperature of methane and equals to 400 K.

Then, the coefficients A and B in the Peng–Robinson equation can be calculated as

$$A = \Omega_a \left[1 + m \left(1 - T_r^{0.5} \right) \right]^2 \frac{P_r}{\left(T_r \right)^2}, \tag{A3}$$

$$B = \Omega_b \frac{P_r}{T_r},\tag{A4}$$

$$m = \begin{cases} 0.37464 + 1.54226\omega - 0.26992\omega^2, & \omega \le 0.49\\ 0.3796 + 1.485\omega - 0.1644\omega^2 + 0.01667\omega^3, & \omega > 0.49, \end{cases}$$
(A5)

$$\begin{cases} \Omega_a = 0.45724 \\ \Omega_b = 0.07780. \end{cases}$$
 (A6)

Finally, substitute the coefficients A and B into the cubic equation regarding the compressibility factor z,

$$z^{3} - (1 - B)z^{2} + (A - 2B - 3B^{2})z - (AB - B^{2} - B^{3}) = 0.$$
 (A7)

By solving Eq. (A7), the density of methane as a function of pressure is presented in Fig. 10.

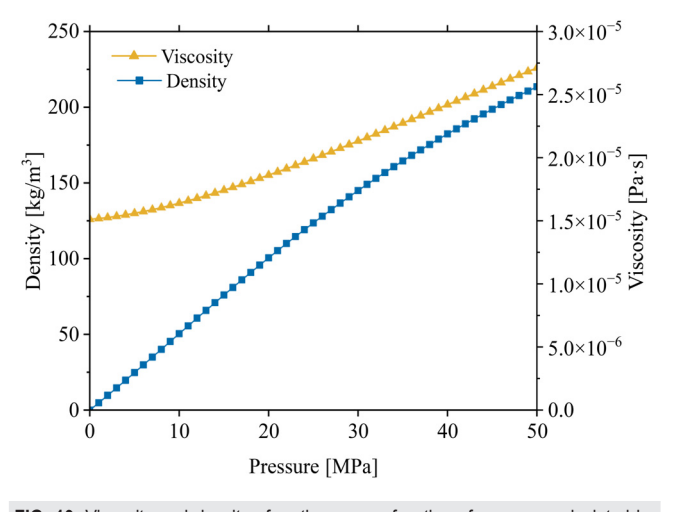


FIG. 10. Viscosity and density of methane as a function of pressure calculated by Lee's relation and PR-EOS, respectively.

APPENDIX B: VISCOSITY CALCULATION PROCEDURE

In this work, we calculate the viscosity of methane by the empirical formula proposed by Lee *et al.* (1966).

$$\mu_g = \frac{Ke^{\left(X\rho_g^Y\right)}}{10000},\tag{B1}$$

where

$$K = \frac{(9.4 + 0.02M_g)T^{1.5}}{(209 + 19M_g + T)},$$
 (B2)

$$X = 3.5 + \frac{986}{T} + 0.001 M_g, \tag{B3}$$

$$Y = 2.4 - 0.2X, (B4)$$

$$M_g = 28.967SG_g,$$
 (B5)

$$\rho_g = \frac{1}{62.428} \times \frac{28.9678G_gP}{Z10.732T},\tag{B6}$$

where ρ_g is the gas density (g/cm³); SG_g is the gas specific gravity, with methane gas specific gravity being 0.5537; P is the gas pressure (psi), where $1 \, \mathrm{Pa} = 0.000 \, 145 \, 04 \, \mathrm{psi}$; T is the temperature (Rankine), where $1 \, \mathrm{K} = 1.8$ Rankine; z is the gas compressibility factor, obtained from the Peng–Robinson Equation of State; M is the gas molecular weight (-), dimensionless; and μ is the gas viscosity, in centipoise (cp). This formula applies within the range of $311 \, \mathrm{K} < T < 444.4 \, \mathrm{K}$ and $0.689 \, \mathrm{MPa} < P < 55.15 \, \mathrm{MPa}$. The viscosity of methane calculated from Eq. (B1) as a function of pressure is presented in Fig. 10.

APPENDIX C: THE IMPACT OF IMAGE COARSENING ON POROSITY AND INTRINSIC PERMEABILITY

In this work, to reduce computational efforts, we resampled the FIB-SEM images of OM by reducing the voxel size from 4 to 32 nm. We compared the number of computational grids, the intrinsic permeability, and the porosity of macropores as decreasing the voxel size, respectively, as shown in Tables VI–VIII.

TABLE VI. The number of computational grids.

Digital rocks	Voxel size 4 nm	Voxel size 8 nm	Voxel size 32 nm
OM-HP	3 467 404	812 675	30 207
OM-MP	2616010	575 147	22 873
OM-LP	3 193 758	748 092	29 105

TABLE VII. The impact of image coarsening on intrinsic permeability.

Digital rocks	Voxel size 4 nm	Voxel size 8 nm	Voxel size 32 nm
OM-HP	1730.65 nD	1351.55 nD	1096.59 nD
OM-MP	18.8811 nD	18.4335 nD	14.8259 nD
OM-LP	17.4787 nD	17.492 nD	14.7062 nD

TABLE VIII. The impact of image coarsening on volume fractions of solid, microporosity, and macropores.

Digital roc	ks	Voxel size 4 nm	Voxel size 8 nm	Voxel size 32 nm
	Solid	1.77%	1.80%	1.69%
OM-HP	Microporosity	73.21%	73.3%	74.44%
	Macropores	25.02%	24.9%	23.87%
	Solid	18.39%	18.38%	18.23%
OM-MP	Microporosity	71.79%	71.85%	72.78%
	Macropores	9.82%	9.77%	8.99%
	Solid	0.06%	0.1%	0.05%
OM-LP	Microporosity	90.4%	90.5%	90.25%
	Macropores	9.52%	9.4%	7.69%

REFERENCES

- Arganda-Carreras, I., Kaynig, V., Rueden, C., Eliceiri, K., Schindelin, J., Cardona, A., and Seung, H., "Trainable Weka Segmentation: A machine learning tool for microscopy pixel classification," Bioinformatics (Oxford, England) 33, 2424–2426 (2017).
- Bauer, D., Youssef, S., Fleury, M., Bekri, S., Rosenberg, E., and Vizika, O., "Improving the estimations of petrophysical transport behavior of carbonate rocks using a dual pore network approach combined with computed microtomography," Transp. Porous Media 94(2), 505–524 (2012).
- Beskok, A. and Karniadakis, G. E., "A model for flows in channels, pipes, and ducts at micro and nano scales," Microscale Thermophys. Eng. 3(1), 43–77 (1999)
- Blunt, M. J., Bijeljic, B., Dong, H., Gharbi, O., Iglauer, S., Mostaghimi, P., Paluszny, A., and Pentland, C., "Pore-scale imaging and modelling," Adv. Water Resour. 51, 197–216 (2013).
- Brinkman, H. C., "A calculation of the viscous force exerted by a flowing fluid on a dense swarm of particles," Appl. Sci. Res. 1(1), 27–34 (1949).
- Bultreys, T., Van Hoorebeke, L., and Cnudde, V., "Multi-scale, micro-computed tomography-based pore network models to simulate drainage in heterogeneous rocks," Adv. Water Resour. 78, 36–49 (2015).
- Chalmers, G. R., Bustin, R. M., and Power, I. M., "Characterization of gas shale pore systems by porosimetry, pycnometry, surface area, and field emission scanning electron microscopy/transmission electron microscopy image analyses: Examples from the Barnett, Woodford, Haynesville, Marcellus, and Doig units," AAPG Bull. 96(6), 1099–1119 (2012).
- Cheng, S. X., Huang, P., Wang, K., Wu, K. L., and Chen, Z. X., "Comprehensive modeling of multiple transport mechanisms in shale gas reservoir production," Fuel 277, 118159 (2020).
- Civan, F., "Effective correlation of apparent gas permeability in tight porous media," Transp. Porous Media 82(2), 375–384 (2010).
- Clarkson, C. R., Solano, N., Bustin, R. M., Bustin, A. M. M., Chalmers, G. R. L., He, L., Melnichenko, Y. B., Radliński, A. P., and Blach, T. P., "Pore structure characterization of North American shale gas reservoirs using USANS/SANS, gas adsorption, and mercury intrusion," Fuel 103, 606–616 (2013).
- Cui, R., Hassanizadeh, S. M., and Sun, S., "Pore-network modeling of flow in shale nanopores: Network structure, flow principles, and computational algorithms," Earth Sci. Rev. 234, 104203 (2022).
- Curtis, M. E., Sondergeld, C. H., Ambrose, R. J., and Rai, C. S., "Microstructural investigation of gas shales in two and three dimensions using nanometer-scale resolution imaging," AAPG Bull. 96(4), 665–677 (2012).
- Dong, H. and Blunt, M., "Pore-network extraction from micro-computerized-tomography images," Phys. Rev. E 80, 036307 (2009).
- Edwards, R. W. J., Celia, M. A., Bandilla, K. W., Doster, F., and Kanno, C. M., "A model to estimate carbon dioxide injectivity and storage capacity for geological sequestration in shale gas wells," Environ. Sci. Technol. 49(15), 9222–9229 (2015).

- Feng, J., Xiong, Q., Qu, Y., and Yang, D., "A new dual-scale pore network model with triple-pores for shale gas simulation," Geoenergy Sci. Eng. 235, 212710 (2024).
- Gensterblum, Y., Ghanizadeh, A., Cuss, R. J., Amann-Hildenbrand, A., Krooss, B. M., Clarkson, C. R., Harrington, J. F., and Zoback, M. D., "Gas transport and storage capacity in shale gas reservoirs—A review. Part A: Transport processes," J. Unconv. Oil Gas Resour. 12, 87–122 (2015).
- Gostick, J. T., "Versatile and efficient pore network extraction method using marker-based watershed segmentation," Phys. Rev. E 96(2), 023307 (2017).
- Guo, B., Ma, L., and Tchelepi, H. A., "Image-based micro-continuum model for gas flow in organic-rich shale rock," Adv. Water Resour. 122, 70–84 (2018).
- He, S., Ning, Y., Chen, T., Liu, H., Wang, H., and Qin, G., "Estimation of transport diffusivity of natural gas in organic matter using molecular dynamics simulation," in SPE Low Perm Symposium, SPE-180198-MS (SPE, 2016).
- Heller, R. and Zoback, M., "Adsorption of methane and carbon dioxide on gas shale and pure mineral samples," J. Unconv. Oil Gas Resour. 8, 14–24 (2014)
- Jiang, Z., van Dijke, M. I. J., Sorbie, K. S., and Couples, G. D., "Representation of multiscale heterogeneity via multiscale pore networks," Water Resour. Res. 49(9), 5437–5449, https://doi.org/10.1002/wrcr.20304 (2013).
- Joyce, S., Hartley, L., Applegate, D., Hoek, J., and Jackson, P., "Multi-scale groundwater flow modeling during temperate climate conditions for the safety assessment of the proposed high-level nuclear waste repository site at Forsmark, Sweden," Hydrolgeol. J. 22(6), 1233–1249 (2014).
- Katz, A. J. and Thompson, A. H., "Quantitative prediction of permeability in porous rock," Phys. Rev. B 34(11), 8179–8181 (1986).
- Kornilov, A. and Safonov, I., "An overview of watershed algorithm implementations in open source libraries," J. Imaging 4, 123 (2018).
- Lee, A. L., Gonzalez, M. H., and Eakin, B. E., "The viscosity of natural gases," J. Pet. Technol. 18(08), 997–1000 (1966).
- Long, S., Feng, D., Li, F., and Du, W., "Prospect analysis of the deep marine shale gas exploration and development in the Sichuan Basin, China," J. Nat. Gas Geosci. 3(4), 181–189 (2018).
- Ma, L., Dowey, P. J., Rutter, E., Taylor, K. G., and Lee, P. D., "A novel upscaling procedure for characterising heterogeneous shale porosity from nanometer-to millimetre-scale in 3D," Energy 181, 1285–1297 (2019).
- Ma, L., Taylor, K. G., Lee, P. D., Dobson, K. J., Dowey, P. J., and Courtois, L., "Novel 3D centimetre-to nano-scale quantification of an organic-rich mudstone: The Carboniferous Bowland Shale, Northern England," Mar. Pet. Geol. 72, 193–205 (2016).
- Ma, X., Wang, H., Zhou, S., Shi, Z., and Zhang, L., "Deep shale gas in China: Geological characteristics and development strategies," Energy Rep. 7, 1903–1914 (2021).
- Medveď, I., Černý, R., Medveď, I., and Černý, R., "Surface diffusion in porous media: A critical review," Microporous Mesoporous Mater. **142**(2), 405 (2011).
- Mehmani, A. and Prodanović, M., "The effect of microporosity on transport properties in porous media," Adv. Water Resour. 63, 104–119 (2014).
- Ning, Y., He, S., Liu, H., Wang, H., and Qin, G., "Upscaling in numerical simulation of shale transport properties by coupling molecular dynamics simulation with lattice Boltzmann method," in *Proceedings of the 4th Unconventional Resources Technology Conference* (URTEC, San Antonio, Texas, 2016).
- Peng, D. and Robinson, D. B., "A new two-constant equation of state," Ind. Eng. Chem. Fund. 15(1), 59-64 (1976).
- Prodanović, M., Mehmani, A., Sheppard, A. P., Agar, S. M., and Geiger, S., "Imaged-based multiscale network modelling of microporosity in carbonates," in Fundamental Controls on Fluid Flow in Carbonates: Current Workflows to Emerging Technologies (Geological Society of London, 2015), Vol. 406.
- Rexer, T. F. T., Mathia, E. J., Aplin, A. C., and Thomas, K. M., "Shale gas exploration and development in China: Current status, geological challenges, and future directions," Energy Fuels 28(5) (2014).
- Ross, D. J. K. and Bustin, R. M., "The importance of shale composition and pore structure upon gas storage potential of shale gas reservoirs," Mar. Pet. Geol. 26(6), 916–927 (2009).
- Schneider, C. A., Rasband, W. S., and Eliceiri, K. W., "NIH Image to ImageJ: 25 years of image analysis," Nat. Methods 9(7), 671–675 (2012).

- Sheng, G., Javadpour, F., and Su, Y., "Dynamic porosity and apparent permeability in porous organic matter of shale gas reservoirs," Fuel 251, 341–351 (2019).
- Sheng, G., Su, Y., Zhao, H., and Liu, J., "A unified apparent porosity/permeability model of organic porous media: Coupling complex pore structure and multimigration mechanism," Adv. Geo-Energy Res. 4(2), 115–125 (2020).
- Shi, B., Jiang, H., Guo, B., Tian, J., and Qin, C.-Z., "Modeling of flow and transport in multiscale digital rocks aided by grid coarsening of microporous domains," J. Hydrol. 633, 131003 (2024).
- Sondergeld, C. H., Ambrose, R. J., Rai, C. S., and Moncrieff, J., "Micro-structural studies of gas shales," in SPE Unconventional Gas Conference, SPE-131771-MS (SPE, 2010).
- Song, W., Yao, J., Ma, J. S., Li, Y., and Han, W. C., "A pore structure based real gas transport model to determine gas permeability in nanoporous shale," Int. J. Heat Mass Transfer 126, 151–160 (2018).
- Song, W., Yao, J., Wang, D., Li, Y., Sun, H., and Yang, Y., "Dynamic pore network modelling of real gas transport in shale nanopore structure," J. Pet. Sci. Eng. 184, 106506 (2020).
- Soulaine, C., Gjetvaj, F., Garing, C., Roman, S., Russian, A., Gouze, P., and Tchelepi, H. A., "The impact of sub-resolution porosity of x-ray microtomography images on the permeability," Transp. Porous Media 113(1), 227–243 (2016)
- Soulaine, C. and Tchelepi, H. A., "Micro-continuum approach for pore-scale simulation of subsurface processes," Transp. Porous Media 113(3), 431–456 (2016).
- Sun, C., Nie, H., Dang, W., Chen, Q., Zhang, G., Li, W., and Lu, Z., "Shale gas exploration and development in China: Current status, geological challenges, and future directions," Energy Fuels 35(8), 6359–6379 (2021).

- Tian, Y., Yan, C., Deng, H., Chen, Q., He, Y., Feng, X., and Li, K., "Apparent permeability of organic matter in shale considering pore size distribution," Chem. Eng. Sci. 266, 118285 (2023).
- Wang, D., Yao, J., Chen, Z., Song, W., Cai, M., Tian, M., Zhang, J., and Xu, W., "Image-based model for dynamic apparent gas permeability in Organic-rich shales," Fuel 318, 123588 (2022).
- Wu, T., Li, X., Zhao, J., and Zhang, D., "Multiscale pore structure and its effect on gas transport in organic-rich shale," Water Resour. Res. 53(7), 5438–5450, https://doi.org/10.1002/2017WR020780 (2017).
- Wu, J. G., Luo, C., Zhong, K. S., Li, Y., Li, G. L., Du, Z. M., and Yang, J. J., "Innovative characterization of organic nanopores in marine shale by the integration of HIM and SEM," Energy 282, 128390 (2023).
- Wu, J., Yuan, Y., Niu, S., Wei, X., and Yang, J., "Multiscale characterization of pore structure and connectivity of Wufeng-Longmaxi shale in Sichuan Basin, China," Mar. Pet. Geol. 120, 104514 (2020).
- Wu, T. and Zhang, D., "Impact of adsorption on gas transport in nanopores," Sci. Rep. 6(1), 23629 (2016).
- Xiong, Q., Baychev, T. G., and Jivkov, A. P., "Review of pore network modelling of porous media: Experimental characterisations, network constructions and applications to reactive transport," J. Contam. Hydrol. 192, 101–117 (2016).
- Yang, Y., Yao, J., Wang, C., Gao, Y., Zhang, Q., An, S., and Song, W., "New pore space characterization method of shale matrix formation by considering organic and inorganic pores," J. Nat. Gas Sci. Eng. 27, 496–503 (2015).
- Zhang, L., Guo, B., Qin, C. Z., and Xiong, Y. Q., "A hybrid pore-network-continuum modeling framework for flow and transport in 3D digital images of porous media," Adv. Water Resour. 190, 104753 (2024).
- Zhu, L., Zhang, C., Zhang, C., Zhou, X., Zhang, Z., Nie, X., Liu, W., and Zhu, B., "Challenges and prospects of digital core-reconstruction research," Geofluids 2019, 1–29.